Orbital Angular Momentum Multiplexed Quantum Dense Coding

Yingxuan Chen,[1,†] Shengshuai Liu,[1,†] Yanbo Lou,[1] and Jietai Jing[1,2,3,4,*]
[1]State Key Laboratory of Precision Spectroscopy, Joint Institute of Advanced Science and Technology, School of Physics and Electronic Science, East China Normal University, Shanghai 200062, China
[2]CAS Center for Excellent in Ultra-intense Laser Science, Shanghai 201800, China
[3]Department of Physics, Zhejiang University, Hangzhou 310027, China
[4]Collaborative Innovation Center of Extreme Optics, Shanxi University, Taiyuan, Shanxi 030006, China

(Received 23 July 2020; accepted 30 July 2021; published 23 August 2021)

To beat the channel capacity limit of conventional quantum dense coding (QDC) with fixed quantum resources, we experimentally implement the orbital angular momentum (OAM) multiplexed QDC (MQDC) in a continuous variable system based on a four-wave mixing process. First, we experimentally demonstrate that the Einstein-Podolsky-Rosen entanglement source coded on OAM modes can be used in a single channel to realize the QDC scheme. Then, we implement the OAM MQDC scheme by using the Einstein-Podolsky-Rosen entanglement source coded on OAM superposition modes. In the end, we make an explicit comparison of channel capacities for four different schemes and find that the channel capacity of the OAM MQDC scheme is substantially enhanced compared to the conventional QDC scheme without multiplexing. The channel capacity of our OAM MQDC scheme can be further improved by increasing the squeezing parameter and the number of multiplexed OAM modes in the channel. Our results open an avenue to construct high-capacity quantum communication networks.

DOI: 10.1103/PhysRevLett.127.093601

Quantum information protocols enabled by quantum entanglement show great advantages in implementing information processing tasks that are impossible with their classical counterparts [1,2]. Quantum teleportation introduced by Bennett *et al.* [3] has been experimentally implemented in optical qubits [4], optical modes [5,6], atomic ensembles [7], trapped atoms [8], and even solid state systems [9]. On par with quantum teleportation, quantum dense coding (QDC) is another fundamental protocol in quantum information [10], one that can, in principle, increase the channel capacity twofold (at most). In this protocol, two bits of classical information can be transmitted by sending one qubit of quantum information if an entangled pair of qubits has been shared previously by the sender and the receiver. QDC was originally introduced in a discrete variable (DV) system and experimentally demonstrated using a source of polarization-entangled photons [11]. Then, the continuous variable (CV) QDC schemes were theoretically proposed [12–15] and experimentally realized [16–18], showing their advantage in enhancing the channel capacity.

A natural question is whether the channel capacity of QDC is already the ultimate limit for channel capacity with fixed quantum resources. Along this line, the channel capacity limit of QDC of a two-dimensional two-photon entanglement has been exceeded by exploiting a four-dimensional two-photon entanglement source in a DV system [19]. Note that the two-photon entanglement was the fixed quantum resource in their experiment. In a CV system, the counterpart of high-dimensional entanglement is a multiplexed entanglement source in which a series of entanglements exists in parallel. Therefore, it is promising to use the multiplexed entanglement source to exceed the channel capacity of QDC in a CV system with fixed quantum resources (the average photon number per bandwidth per second in the channel). As one of the most fundamental physical quantities, the orbital angular momentum (OAM) of light [20] has been used to realize multiplexing [21–23] and increase the capacity of free space [21] or fiber [22] communication links because the OAM of light could, in principle, support an infinite number of optical modes. Very recently, OAM multiplexed bipartite [24] and tripartite [25] entanglements have been experimentally generated. Such multiplexed resources are promising for demonstrating the high-capacity quantum information protocols. In this Letter, we experimentally implement, based on the four-wave mixing (FWM) process in an atomic ensemble [24–29], an OAM multiplexed QDC scheme (MQDC) for a CV system. We first demonstrate that the QDC scheme can be realized when the Einstein-Podolsky-Rosen (EPR) entanglement source is coded on an OAM mode with a single topological charge l and measure the signal-to-noise ratios (SNRs), which are needed for the derivation of the channel capacity. Then, we implement an OAM MQDC scheme with an entanglement source coded on the OAM superposition modes and measure the corresponding SNRs. In the end, we make an explicit comparison of the channel capacities of different schemes using the

measured SNRs. Compared to a conventional QDC scheme without multiplexing, the channel capacity of our OAM MQDC scheme is substantially enhanced.

The detailed experimental setup of our scheme is shown in Fig. 1(a). The double-Λ energy level configuration is shown in Fig. 1(b). The frequency of the Ti sapphire laser is blue detuned by about 1 GHz from the $D1$ line ($5S_{1/2}, F = 2 \rightarrow 5P_{1/2}$, 795 nm) of ^{85}Rb, which is called one-photon detuning (Δ). A polarization beam splitter is used to divide the laser into two. The strong one with a beam waist of about 860 μm and power of about 140 mW serves as the pump beam. The weak one is used to generate the seeded probe beam, which is red detuned by 3.04 GHz from the pump beam via an acousto-optic modulator. This means that the probe beam is red detuned by 4 MHz from the ^{85}Rb ground-state hyperfine splitting of 3.036 GHz, which is called two-photon detuning (δ) and shown in Fig. 1(b). Then, the probe beam is coded on a Laguerre-Gauss (LG) mode (LG_l mode or $LG_l + LG_{-l}$ superposition mode) by a spatial light modulator. (The OAM modes involved in the experiment are of high quality. See the Supplemental Material, Sec. C, for the mode analysis of the generated OAM modes [30].) The power of the seeded probe beam coded on the LG mode is about 2 μW, and it crosses with the pump beam at the center of a 12 mm hot ^{85}Rb vapor cell to generate the EPR entanglement source by the FWM process [24]. The angle θ between the pump and probe beams is about 7 mrad. The Hamiltonian of the system can be expressed as

$$\hat{H} = \sum_l i\hbar r_l \hat{b}^{\dagger}_{\mathrm{pr},l} \hat{b}^{\dagger}_{\mathrm{conj},-l} + \mathrm{H.c.} \tag{1}$$

r_l denotes the interaction strength, which is dependent on the topological charge l. $\hat{b}^{\dagger}_{\mathrm{pr},l}$ and $\hat{b}^{\dagger}_{\mathrm{conj},-l}$ are the creation operators associated with the probe and conjugate beams, respectively. Then, the output fields after the FWM process can be expressed as

$$\begin{aligned} \hat{b}_{\mathrm{pr},l}(t) &= \sqrt{G_{\mathrm{pr},l}}\hat{b}_{\mathrm{pr},l} + \sqrt{G_{\mathrm{pr},l}-1}\hat{b}^{\dagger}_{\mathrm{conj},-l}, \\ \hat{b}_{\mathrm{conj},-l}(t) &= \sqrt{G_{\mathrm{pr},l}-1}\hat{b}^{\dagger}_{\mathrm{pr},l} + \sqrt{G_{\mathrm{pr},l}}\hat{b}_{\mathrm{conj},-l}, \end{aligned} \tag{2}$$

where $G_{\mathrm{pr},l} = \cos h^2(r_l t)$ is the gain of the FWM process and t is the interaction time.

As a result, the EPR entangled beams are generated. Based on Eq. (2), the variances of the sum or difference combinations of the amplitude and phase quadratures can be expressed as

$$\begin{aligned} \mathrm{Var}(\hat{X}_{\mathrm{pr},l} + \hat{X}_{\mathrm{conj},-l}) &= 4G_{\mathrm{pr},l} - 2 + 4\sqrt{G_{\mathrm{pr},l}(G_{\mathrm{pr},l}-1)}, \\ \mathrm{Var}(\hat{X}_{\mathrm{pr},l} - \hat{X}_{\mathrm{conj},-l}) &= 4G_{\mathrm{pr},l} - 2 - 4\sqrt{G_{\mathrm{pr},l}(G_{\mathrm{pr},l}-1)}, \\ \mathrm{Var}(\hat{Y}_{\mathrm{pr},l} + \hat{Y}_{\mathrm{conj},-l}) &= 4G_{\mathrm{pr},l} - 2 - 4\sqrt{G_{\mathrm{pr},l}(G_{\mathrm{pr},l}-1)}, \\ \mathrm{Var}(\hat{Y}_{\mathrm{pr},l} - \hat{Y}_{\mathrm{conj},-l}) &= 4G_{\mathrm{pr},l} - 2 + 4\sqrt{G_{\mathrm{pr},l}(G_{\mathrm{pr},l}-1)}, \end{aligned} \tag{3}$$

where $\hat{X}_{\mathrm{pr},l} = \hat{b}_{\mathrm{pr},l} + \hat{b}^{\dagger}_{\mathrm{pr},l}$ and $\hat{X}_{\mathrm{conj},-l} = \hat{b}_{\mathrm{conj},-l} + \hat{b}^{\dagger}_{\mathrm{conj},-l}$ and $\hat{Y}_{\mathrm{pr},l} = i(\hat{b}^{\dagger}_{\mathrm{pr},l} - \hat{b}_{\mathrm{pr},l})$ and $\hat{Y}_{\mathrm{conj},-l} = i(\hat{b}^{\dagger}_{\mathrm{conj},-l} - \hat{b}_{\mathrm{conj},-l})$ are the amplitude and phase quadratures of the probe and conjugate beams, respectively. $\mathrm{Var}(\hat{X}_{\mathrm{pr},l} - \hat{X}_{\mathrm{conj},-l})$ and $\mathrm{Var}(\hat{Y}_{\mathrm{pr},l} + \hat{Y}_{\mathrm{conj},-l})$ are both lower than the shot-noise limit (SNL) defined by the vacuum fluctuation when $G_{\mathrm{pr},l} > 1$. Then, the probe beam (EPR1) is distributed to the Alice station, where the classical amplitude and phase signals are encoded on it through an amplitude modulator and phase modulator, respectively. The power of signals modulated on amplitude quadrature $V_{SX,l}$ and phase quadrature $V_{SY,l}$ is set to $V_{SX,l} = V_{SY,l} = V_S$. At the Bob station, the signals are decoded with the help of the other EPR beam [the conjugate beam (EPR2)] by two balanced homodyne detections (BHDs). The local oscillators are obtained by implementing a similar setup a few millimeters below the current corresponding beams. The two photocurrents obtained from the two BHDs are sent into a hybrid junction, whose outputs are analyzed by two spectrum analyzers. Both analyzers are set to a 30 kHz resolution bandwidth and a 300 Hz video bandwidth. When the pump of the FWM process is blocked, the above procedure can be regarded as a coherent state scheme with an LG_l mode or

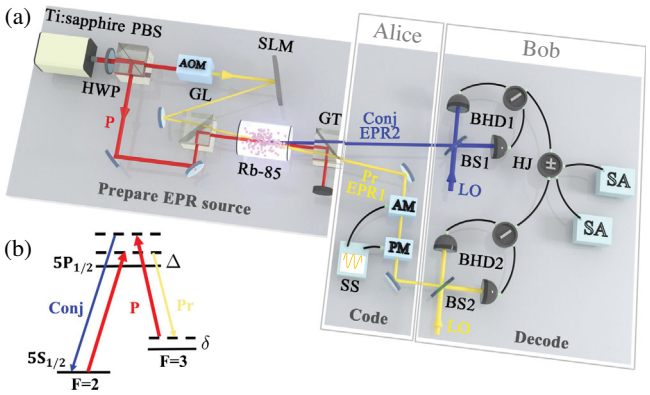

FIG. 1. The detailed experimental setup for a OAM MQDC scheme. (a) OAM MQDC scheme. HWP: half-wave plate; PBS: polarization beam splitter; AOM: acousto-optic modulator; SLM: spatial light modulator; GL: Glan-Laser polarizer; Rb-85: hot ^{85}Rb vapor cell; GT: Glan-Thompson polarizer; AM: amplitude modulator; PM: phase modulator; SS: signal source; BS1 and BS2: 50:50 beam splitters; BHD1 and BHD2: balanced homodyne detections; HJ: hybrid junction; SA: spectrum analyzer; P: pump beam; Pr: probe beam; Conj: conjugate beam; LO: local oscillator. (b) Energy level diagram of the double-Λ scheme in the $D1$ line of ^{85}Rb. Δ: one-photon detuning; δ: two-photon detuning.

$LG_l + LG_{-l}$ superposition mode. We treat these coherent states as the classical counterparts of conventional QDC or OAM MQDC.

We first introduce the channel capacity theoretically before elaborating the experimental results. Generally, the channel capacity of quantum states with Gaussian probability distributions can be calculated as [15]

$$C = \frac{1}{2}\log_2\left[1 + \frac{S}{N}\right], \tag{4}$$

where S is the signal power and N is the noise power (variance). The SNR is given by $SNR = S/N$. In order to make a fair comparison of the channel capacities of different schemes, the average photon number per bandwidth per second $\bar{n}$ in the channel must be fixed. When the power of modulation signals satisfies the large power modulation situation, the average photon number is only related to the power of modulation signals. (See the Supplemental Material, Sec. A, for a detailed introduction of the large power modulation situation (power modulation is much greater than 1) [30].) Therefore, we can keep the average photon number $\bar{n}$ fixed for different schemes by keeping the power of modulation signals fixed to V_S. The derivations for the channel capacities of four different schemes (a coherent state scheme with LG_l mode, a coherent state scheme with $LG_l + LG_{-l}$ superposition mode, a conventional QDC scheme, and an OAM MQDC scheme) are shown in detail in Sec. A of the Supplemental Material [30]. The SNRs required for deriving the corresponding channel capacities can be obtained from the noise power spectra measured by the BHDs.

For the seeded probe beam coded on the LG_1 mode, the output noise power spectra measured by the BHDs are shown in Figs. 2(a) and 2(b). Figure 2(a) [2(b)] shows the output noise power spectrum of an amplitude quadrature (phase quadrature) with the phases of the BHDs locked to 0 ($\pi/2$). The blue dashed traces in Figs. 2(a) and 2(b) are the normalized SNLs with modulation signals. The peak of the blue dashed trace in Fig. 2(a) [2(b)] at 1.5 MHz is the signal modulated on the probe beam by the amplitude modulator (phase modulator) at the Alice station. These peaks are set to about 21 dB above the SNLs to satisfy the situation of large power modulation, as mentioned above. The red traces show SNLs. The red traces and the peaks of the blue dashed traces give the SNR results for a coherent state scheme with the LG_1 mode. The orange traces in Figs. 2(a) and 2(b) are $\mathrm{Var}(\hat{X}_{\mathrm{pr},1} - \hat{X}_{\mathrm{conj},-1})$ and $\mathrm{Var}(\hat{Y}_{\mathrm{pr},1} + \hat{Y}_{\mathrm{conj},-1})$ with modulation signals, respectively. The peaks on the noise spectra at 1.5 MHz are the signals modulated on the probe beam (EPR1), which are also about 21 dB above the SNLs. The black traces in Figs. 2(a) and 2(b) show $\mathrm{Var}(\hat{X}_{\mathrm{pr},1} - \hat{X}_{\mathrm{conj},-1})$ and $\mathrm{Var}(\hat{Y}_{\mathrm{pr},1} + \hat{Y}_{\mathrm{conj},-1})$, respectively. The black traces and the peaks of the orange traces can give the SNR results for the conventional QDC scheme with the seeded probe beam coded on the LG_1 mode.

For the coherent state scheme with LG_1 mode, we can obtain the signal power (S) and the noise power (N) from

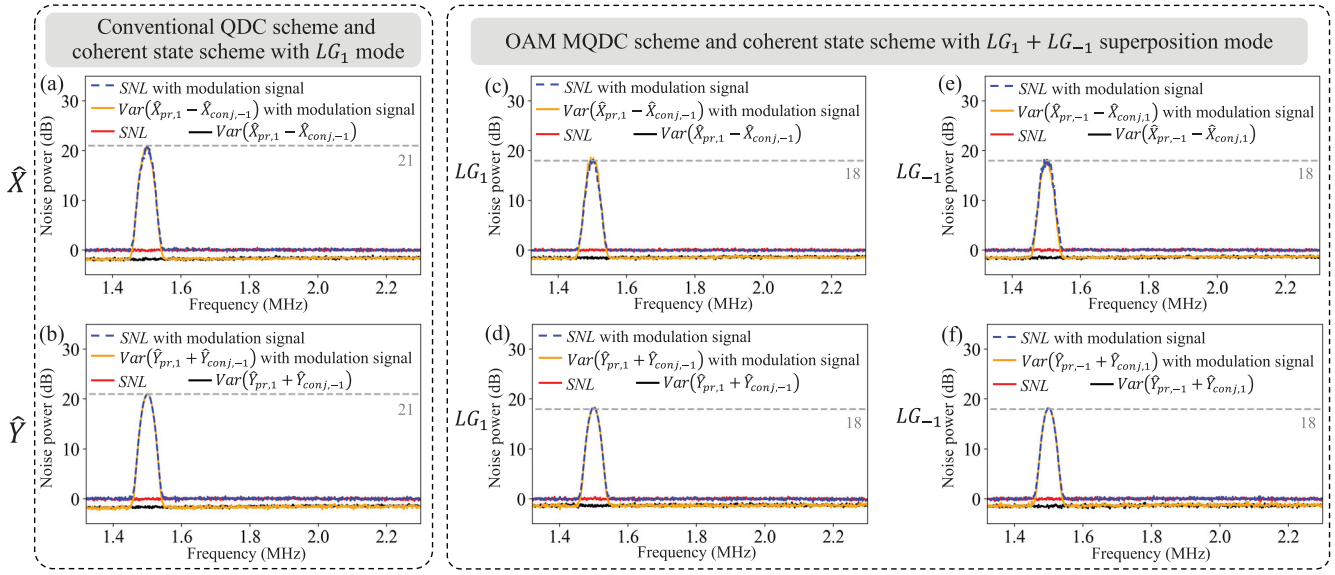

FIG. 2. The measured output noise power spectra. (a) and (b) show the measured noise power spectra for a coherent state scheme with LG_1 mode (blue and red traces) and a QDC scheme with the seeded probe beam coded on the LG_1 mode (orange and black traces). (c)–(f) show the measured noise power spectra for a coherent state scheme with $LG_1 + LG_{-1}$ superposition mode (blue and red traces) and a OAM MQDC scheme with the seeded probe beam coded on the $LG_1 + LG_{-1}$ superposition mode (orange and black traces). (a),(c),(e) show the measured noise power spectra of the amplitude quadrature, while (b),(d),(f) show the measured noise power spectra of the phase quadrature. The vertical scale is normalized to the SNL.

the red traces and the peaks of the blue dashed traces. Specifically, S is the peak value of the blue dashed trace minus the value of the red trace at 1.5 MHz. N is the value of the red trace at 1.5 MHz. By calculation, the SNRs are 20.8 ± 0.4 dB $(V_S/V_{NVX,1})$ and 21.0 ± 0.1 dB $(V_S/V_{NVY,1})$ for the amplitude quadrature and phase quadrature, respectively. $V_{NVX,l}$ and $V_{NVY,l}$ are the variances of the amplitude quadrature and phase quadrature for each OAM mode case, respectively. For the conventional QDC scheme with the seeded probe beam coded on the LG_1 mode, we can obtain S and N from the black traces and the peaks of orange traces at 1.5 MHz. The SNRs are 22.4 ± 0.4 dB $(V_S/V_{NEX,1})$ and 22.6 ± 0.2 dB $(V_S/V_{NEY,1})$ for the amplitude quadrature and phase quadrature, respectively. $V_{NEX,l}$ and $V_{NEY,l}$ are the variances of the amplitude quadrature $[\mathrm{Var}(\hat{X}_{\mathrm{pr},l} - \hat{X}_{\mathrm{conj},-l})]$ and phase quadrature $[\mathrm{Var}(\hat{Y}_{\mathrm{pr},l} + \hat{Y}_{\mathrm{conj},-l})]$ for the EPR entangled beams, respectively. Similarly, the corresponding results for the seeded probe beam coded on the LG_l mode for the cases of $l = -2, -1, 0, 2$ are shown in Fig. S1 of the Supplemental Material [30].

When the seeded probe beam is coded on the $LG_1 + LG_{-1}$ superposition mode, based on Eqs. (6) and (8) in Sec. A of the Supplemental Material [30], we need to measure the SNRs for the case of the probe beam coded on LG_1 and the case of the probe beam coded on LG_{-1} to derive the channel capacities. Because that different OAM modes are orthogonal with each other, we can measure the SNRs by changing the OAM modes of the local oscillators correspondingly. Note that multiplexing is usually used to describe two completely unrelated signals that are combined in the same channel, and superposition is normally used to denote a coherent superposition of states whose phase relationship is kept constant. Because of the fact that the channel capacity of OAM MQDC is independent of the phase relationship of the two multiplexed modes, such difference between multiplexing and superposition has no effect on implementing OAM MQDC. Therefore, we can implement OAM MQDC by using the OAM superposition mode. The experimental results are shown in Figs. 2(c)–(f). Figure 2(c) [2(d)] shows the noise spectrum of the amplitude (phase) quadrature for the case of the probe beam coded on the LG_1 mode. The phases of BHDs are locked to 0 and $\pi/2$ for Figs. 2(c) and 2(d), respectively. The blue dashed traces in Figs. 2(c) and 2(d) are the SNLs with modulation signals. The red traces in Figs. 2(c) and 2(d) are the SNLs. The orange traces in Figs. 2(c) and 2(d) are $\mathrm{Var}(\hat{X}_{\mathrm{pr},1} - \hat{X}_{\mathrm{conj},-1})$ and $\mathrm{Var}(\hat{Y}_{\mathrm{pr},1} + \hat{Y}_{\mathrm{conj},-1})$ with modulation signals. The black traces in Figs. 2(c) and 2(d) are $\mathrm{Var}(\hat{X}_{\mathrm{pr},1} - \hat{X}_{\mathrm{conj},-1})$ and $\mathrm{Var}(\hat{Y}_{\mathrm{pr},1} + \hat{Y}_{\mathrm{conj},-1})$, respectively. For the case of the probe beam coded on LG_{-1}, the corresponding results are shown in Figs. 2(e) and 2(f). Because the average photon number in the channel must be fixed for different schemes, we set the peaks on the noise spectra of Figs. 2(c)–(f) at about 18 dB above the SNLs, while the peaks on the noise spectra of Figs. 2(a) and 2(b) are set to about 21 dB above the SNLs. The 3 dB difference between them corresponds to a twofold difference in linear scale.

The red traces and the peaks of the blue dashed traces at 1.5 MHz in Figs. 2(c)–(f) can give the SNR results for the coherent state scheme with the $LG_1 + LG_{-1}$ superposition mode. By calculation, the SNRs are 18.1 ± 0.4 dB $(V_S/2/V_{NVX,1})$ and 18.2 ± 0.1 dB $(V_S/2/V_{NVY,1})$ for the amplitude quadrature and phase quadrature in Figs. 2(c) and 2(d), respectively. The SNRs are 18.2 ± 0.2 dB $(V_S/2/V_{NVX,-1})$ and 18.0 ± 0.2 dB $(V_S/2/V_{NVY,-1})$ for the amplitude quadrature and phase quadrature in Figs. 2(e) and 2(f), respectively. The black traces and the peaks of the orange traces at 1.5 MHz in Figs. 2(c)–(f) can give the SNR results for the OAM MQDC scheme with the seeded probe beam coded on the $LG_1 + LG_{-1}$ superposition mode. By calculation, the SNRs are 19.7 ± 0.3 dB $(V_S/2/V_{NEX,1})$ and 19.7 ± 0.2 dB $(V_S/2/V_{NEY,1})$ for the amplitude quadrature and phase quadrature in Figs. 2(c) and 2(d), respectively. The SNRs are 19.4 ± 0.2 dB $(V_S/2/V_{NEX,-1})$ and 19.6 ± 0.2 dB $(V_S/2/V_{NEY,-1})$ for the amplitude quadrature and phase quadrature in Figs. 2(e) and 2(f), respectively. Similarly, the corresponding results with the seeded probe beam coded on the $LG_2 + LG_{-2}$ superposition mode are shown in Fig. S2 of the Supplemental Material [30].

Using the measured SNRs mentioned above and the channel capacity formula of each scheme given in Sec. A of the Supplemental Material [30], we can derive the corresponding channel capacity. The channel capacities for the four different schemes are shown in Fig. 3. The orange bars

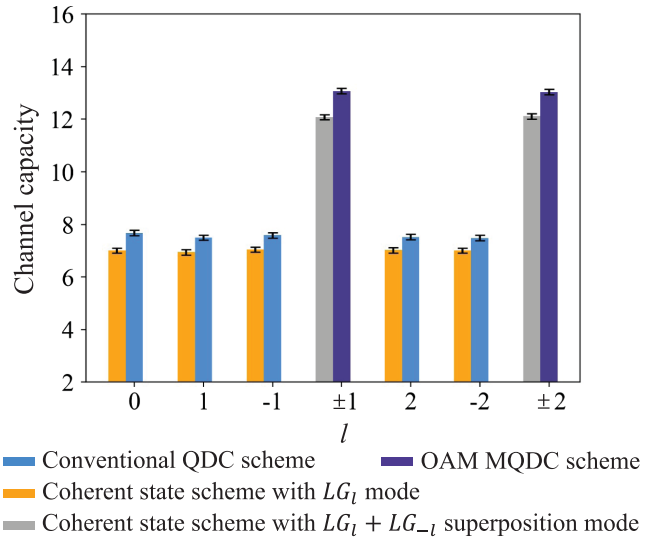

FIG. 3. The channel capacities for different schemes vs topological charges l. The error bars are obtained from the standard deviations of multiple repeated measurements.

show the channel capacities for the coherent state scheme with LG_l mode ($l = -2, -1, 0, 1, 2$). The gray bars show the channel capacities for the coherent state scheme with $LG_l + LG_{-l}$ superposition mode ($l = 1, 2$). The blue bars show the channel capacities of the conventional QDC scheme with the seeded probe beam coded on the LG_l mode ($l = -2, -1, 0, 1, 2$). The dark purple bars show the channel capacities of the OAM MQDC scheme with the seeded probe beam coded on the $LG_l + LG_{-l}$ superposition mode ($l = 1, 2$). We can see that, with the help of an EPR entanglement source, the channel capacities of the conventional QDC schemes (blue bars) exceed those of coherent state schemes (orange bars), and the enhancement is about 0.4 dB for the case of $l = 0$. More importantly, when the seeded probe beam is coded on the $LG_1 + LG_{-1}$ mode, the channel capacity of the OAM MQDC scheme (dark purple bars) is greatly improved, obtaining a 2.4 dB channel capacity enhancement compared to the corresponding conventional QDC scheme (blue bars). In other words, our OAM MQDC scheme can exceed the corresponding conventional QDC scheme in terms of the channel capacity with fixed quantum resources.

Moreover, our OAM MQDC scheme (dark purple bars) achieves a 2.7 dB channel capacity enhancement compared to the classical counterpart of using a coherent state (orange bars). Such a 3 dB level of channel capacity enhancement is hard to reach for conventional QDC in both CV and DV systems. To reach this doubling of channel capacity, one should be able to deterministically discriminate all four Bell states for conventional DV QDC [32,33] or generate an ultrahigh level of squeezing for conventional CV QDC [12], both of which are extremely difficult to implement. Therefore, our results explicitly show the great advantage of OAM MQDC for substantially enhancing the channel capacity.

In conclusion, we have experimentally demonstrated that an EPR entanglement source with a probe beam coded on the LG_l mode ($l = -2, -1, 0, 1, 2$) can be used in a single channel to accomplish the conventional QDC scheme. Moreover, we have realized a OAM MQDC scheme by using an EPR entanglement source with the probe beam coded on the $LG_l + LG_{-l}$ superposition mode ($l = 1, 2$). In the end, with the measured SNRs, we have made an explicit comparison of channel capacities for four different schemes and found that, with the help of an EPR entanglement source, the channel capacities of a conventional QDC scheme exceed that of a coherent state scheme. More importantly, we find that the channel capacity of a OAM MQDC scheme is significantly enhanced compared to the conventional QDC scheme. Our results clearly show the ability of OAM multiplexing to substantially enhance the channel capacity of CV quantum information protocols. The channel capacity of our scheme can be further improved by increasing the squeezing parameter and the number of multiplexed OAM modes in the channel. It can also be further improved by combining OAM multiplexing with other types of multiplexing technologies such as wavelength multiplexing [34–39].

This work was funded by the Innovation Program of Shanghai Municipal Education Commission (Grant No. 2021-01-07-00-08-E00100), the National Natural Science Foundation of China (11874155, 91436211, 11374104), the Basic Research Project of Shanghai Science and Technology Commission (20JC1416100), the Natural Science Foundation of Shanghai (17ZR1442900), the Minhang Leading Talents (201971), the Program of Scientific and Technological Innovation of Shanghai (17JC1400401), the Shanghai Sailing Program (21YF1410800), the National Basic Research Program of China (2016YFA0302103), the Shanghai Municipal Science and Technology Major Project (2019SHZDZX01), and the 111 Project (B12024).

Note added.—We recently became aware of an independent experiment using frequency multiplexing [40].

*Corresponding author.
jtjing@phy.ecnu.edu.cn
†These authors contributed equally to this work.

[1] S. L. Braunstein and P. van Loock, Rev. Mod. Phys. **77**, 513 (2005).
[2] C. Weedbrook, S. Pirandola, R. García-Patrón, N. J. Cerf, T. C. Ralph, J. H. Shapiro, and S. Lloyd, Rev. Mod. Phys. **84**, 621 (2012).
[3] C. H. Bennett, G. Brassard, C. Crépeau, R. Jozsa, A. Peres, and W. K. Wootters, Phys. Rev. Lett. **70**, 1895 (1993).
[4] D. Bouwmeester, J. Pan, K. Mattle, M. Eibl, H. Weinfurter, and A. Zeilinger, Nature (London) **390**, 575 (1997).
[5] A. Furusawa, J. L. Srensen, S. L. Braunstein, C. A. Fuchs, H. J. Kimble, and E. S. Polzik, Science **282**, 706 (1998).
[6] M. Huo, J. Qin, J. Cheng, Z. Yan, Z. Qin, X. Su, X. Jia, C. Xie, and K. Peng, Sci. Adv. **4**, eaas9401 (2018).
[7] M. A. Nielsen, E. Knill, and R. Laflamme, Nature (London) **396**, 52 (1998).
[8] S. Olmschenk, D. N. Matsukevich, P. Maunz, D. Hayes, L. Duan, and C. Monroe, Science **323**, 486 (2009).
[9] L. Steffen, Y. Salathe, M. Oppliger, P. Kurpiers, M. Baur, C. Lang, C. Eichler, G. Puebla-Hellmann, A. Fedorov, and A. Wallraff, Nature (London) **500**, 319 (2013).
[10] C. H. Bennett and S. J. Wiesner, Phys. Rev. Lett. **69**, 2881 (1992).
[11] K. Mattle, H. Weinfurter, P. G. Kwiat, and A. Zeilinger, Phys. Rev. Lett. **76**, 4656 (1996).
[12] S. L. Braunstein and H. J. Kimble, Phys. Rev. A **61**, 042302 (2000).
[13] J. Zhang and K. Peng, Phys. Rev. A **62**, 064302 (2000).
[14] M. Ban, J. Opt. B: Quantum Semiclass. Opt. **1**, L9 (1999).
[15] T. C. Ralph and E. H. Huntington, Phys. Rev. A **66**, 042321 (2002).
[16] X. Li, Q. Pan, J. Jing, J. Zhang, C. Xie, and K. Peng, Phys. Rev. Lett. **88**, 047904 (2002).

[17] J. Jing, J. Zhang, Y. Yan, F. Zhao, C. Xie, and K. Peng, Phys. Rev. Lett. **90**, 167903 (2003).
[18] J. Mizuno, K. Wakui, A. Furusawa, and M. Sasaki, Phys. Rev. A **71**, 012304 (2005).
[19] X. Hu, Y. Guo, B. Liu, Y. Huang, C. Li, and G. Guo, Sci. Adv. **4**, eaat9304 (2018).
[20] L. Allen, M. W. Beijersbergen, R. J. C. Spreeuw, and J. P. Woerdman, Phys. Rev. A **45**, 8185 (1992).
[21] J. Wang, J. Yang, I. M. Fazal, N. Ahmed, Y. Yan, H. Huang, Y. Ren, Y. Yue, S. Dolinar, M. Tur, and A. E. Willner, Nat. Photonics **6**, 488 (2012).
[22] N. Bozinovic, Y. Yue, Y. Ren, M. Tur, P. Kristensen, H. Huang, A. E. Willner, and S. Ramachandran, Science **340**, 1545 (2013).
[23] A. Trichili, A. B. Salem, A. Dudley, M. Zghal, and A. Forbes, Opt. Lett. **41**, 3086 (2016).
[24] X. Pan, S. Yu, Y. Zhou, K. Zhang, K. Zhang, S. Lv, S. Li, W. Wang, and J. Jing, Phys. Rev. Lett. **123**, 070506 (2019).
[25] S. Li, X. Pan, Y. Ren, H. Liu, S. Yu, and J. Jing, Phys. Rev. Lett. **124**, 083605 (2020).
[26] S. Liu, Y. Lou, and J. Jing, Phys. Rev. Lett. **123**, 113602 (2019).
[27] C. F. McCormick, V. Boyer, E. Arimondo, and P. D. Lett, Opt. Lett. **32**, 178 (2007).
[28] V. Boyer, A. M. Marino, R. C. Pooser, and P. D. Lett, Science **321**, 544 (2008).
[29] A. M. Marino, R. C. Pooser, V. Boyer, and P. D. Lett, Nature (London) **457**, 859 (2009).
[30] See the Supplemental Material, which includes Ref. [31], at http://link.aps.org/supplemental/10.1103/PhysRevLett.127.093601 for the introduction of the large power modulation situation, the derivation of channel capacities for four different schemes, the output noise power spectra of different schemes, and the OAM mode analysis.
[31] S. Liu, Y. Lou, and J. Jing, Nat. Commun. **11**, 3875 (2020).
[32] J. T. Barreiro, T.-C. Wei, and P. G. Kwiat, Nat. Phys. **4**, 282 (2008).
[33] B. P. Williams, R. J. Sadlier, and T. S. Humble, Phys. Rev. Lett. **118**, 050501 (2017).
[34] M. Pysher, Y. Miwa, R. Shahrokhshahi, R. Bloomer, and O. Pfister, Phys. Rev. Lett. **107**, 030505 (2011).
[35] M. Chen, N. C. Menicucci, and O. Pfister, Phys. Rev. Lett. **112**, 120505 (2014).
[36] J. Roslund, R. M. de Araújo, S. Jiang, C. Fabre, and N. Treps, Nat. Photonics **8**, 109 (2014).
[37] F. A. S. Barbosa, A. S. Coelho, L. F. Muñoz-Martínez, L. Ortiz-Gutiérrez, A. S. Villar, P. Nussenzveig, and M. Martinelli, Phys. Rev. Lett. **121**, 073601 (2018).
[38] M. Grimau Puigibert, G. H. Aguilar, Q. Zhou, F. Marsili, M. D. Shaw, V. B. Verma, S. W. Nam, D. Oblak, and W. Tittel, Phys. Rev. Lett. **119**, 083601 (2017).
[39] C. Joshi, A. Farsi, S. Clemmen, S. Ramelow, and A. L. Gaeta, Nat. Commun. **9**, 847 (2018).
[40] S. Shi, L. Tian, Y. Wang, Y. Zheng, C. Xie, and K. Peng, Phys. Rev. Lett. **125**, 070502 (2020).